future pharmacology

MDPI

Article

A Synergistic Antibacterial Platform Combining Low–Temperature Photothermal Therapy and Antibiotic Therapy

Qiming Zhang [1], Lei Chang [2], Caixia Sun [1], Wanchao Zuo [1], Shibo Zhang [1], Cong Liu [1], Shuyue Deng [1], Pengcheng Wu [1], Panpan Dai [1], Jianjun Dai [1,3,4,*] and Yanmin Ju [1,*]

[1] College of Pharmacy, China Pharmaceutical University, Nanjing 211198, China
[2] Guangzhou Laboratory, Department of Fundamental Research, Guangzhou 510005, China
[3] MOE Joint International Research Laboratory of Animal Health and Food Safety, College of Veterinary Medicine, Nanjing Agricultural University, Nanjing 210095, China
[4] Laboratory of Animal Bacteriology, Ministry of Agriculture, College of Veterinary Medicine, Nanjing Agricultural University, Nanjing 210095, China
* Correspondence: jjdai@cpu.edu.cn (J.D.); juyanmin@cpu.edu.cn (Y.J.)

Abstract: Antimicrobial resistance has brought great burden to global public health. Alternative strategies are needed to reduce the development of drug resistance. Herein, we have developed an effective synergistic antibacterial strategy combining low–temperature photothermal therapy (LT–PTT) with antibiotic therapy, improving the bactericidal efficiency to avoid antimicrobial resistance. Copper sulfide templated with bovine serum albumin (CuS–BSA) nanoparticles were selected as the photothermal agent, and co–loaded into the hydrogel (Gel) with mupirocin. The Gel could slow down the release rate of CuS–BSA and mupirocin, thereby prolonging the effective drug reaction time. More importantly, when applying near–infrared laser irradiation, the antibacterial activity of the platform could be enhanced greatly by LT–PTT effect of CuS–BSA nanoparticles. In vitro and in vivo results both confirmed that the antibacterial efficacy of the synergistic therapeutic strategy was improved greatly with complete bacterial removal. Overall, this platform has posed a potential strategy to reduce the development of drug resistance and improve patient compliance.

Keywords: antimicrobial resistance; synergistic platform; low–temperature photothermal therapy; antibiotic therapy

Citation: Zhang, Q.; Chang, L.; Sun, C.; Zuo, W.; Zhang, S.; Liu, C.; Deng, S.; Wu, P.; Dai, P.; Dai, J.; et al. A Synergistic Antibacterial Platform Combining Low–Temperature Photothermal Therapy and Antibiotic Therapy. *Future Pharmacol.* **2023**, *3*, 180–197. https://doi.org/10.3390/futurepharmacol3010013

Academic Editor: Fabrizio Schifano

Received: 19 November 2022
Revised: 18 January 2023
Accepted: 3 February 2023
Published: 7 February 2023

1. Introduction

Many kinds of severe diseases, such as erysipelas, cellulitis, and even septicemia, occur due to bacterial infections [1–3]. The usage of antibiotics is the most common clinical treatment for bacterial infection [4]. However, antimicrobial resistance has become the main reason for death caused by bacterial infections, directly leading to 1.27 million deaths in 2019, which is a complex threat to the global public health [5]. An inappropriate dose of antibiotics during the long–term treatment are important reasons for antimicrobial resistance [6]. Therefore, there is an urgent need to develop optimization strategies to prolong the service life of antibiotics.

Low–temperature photothermal therapy (LT–PTT) utilizes photothermal agents to convert the absorbed photon energy into a mild temperature elevation maintained at about 45 °C via photothermal effect, which has attracted increasing attention [7]. Compared to high–temperature photothermal therapy, LT–PTT could effectively protect surrounding healthy tissues from inflammation and irreversible high temperature damage [8,9]. Significantly, LT–PTT holds great promise in antibacterial treatment as it would inhibit the activity of bacteria and strengthen the therapeutic effect of drugs [10,11]. For example, recent studies have revealed that LT–PTT re–sensitized *MRSA* to aminoglycoside antibiotics

as it could inhibit the catalytic activity of 2–aminoglycoside phosphotransferase in bacteria related to antimicrobial resistance [12]. Various alternative materials can serve as NIR light–activated photothermal therapeutic agents, such as indocyanine green, cyanine dye, copper sulfide nanoparticles, and so on, due to the strong absorption and photothermal stability when exposed to NIR laser [13–15]. Therefore, the synergistic strategy combining LT–PTT with antibiotic therapy is a great promising synergistic antibacterial platform.

Considering sustained drug release can maintain the local concentration and prolong the effective time of drugs, hydrogel (Gel) with a three–dimensional network structure is usually an ideal biomedical material for drug loading and delivering [16]. Apart from its biocompatibility, Gel can also absorb the exudate of the wound, maintain the wetness of the wound surface, and provide a suitable healing environment for the wound [17,18]. The Gel crosslinked by partially oxidized hyaluronic acid (oHA) and adipic acid dihydrazide (ADH) has wide applications in biomedicine, with physiological functions of promoting wound healing and tissue regeneration [19–22]. Notably, it is also an easily gelled material which can quickly transform from a liquid form to a gel state at room temperature [23]. Therefore, it is an ideal material as a carrier to load and release drugs.

Herein, we developed an effective synergistic antibacterial strategy combining LT–PTT with antibiotic therapy through Gel. Copper sulfide templated with bovine serum albumin (CuS–BSA) nanoparticles were applied as a stable photothermal agent. CuS–BSA and mupirocin were loaded into Gel crosslinked by oHA and ADH to form the platform named as C/M@Gel. With NIR laser irradiation, the whole system could reduce the dosage of antibiotics greatly while ensuring an excellent germicidal efficacy. As shown in Scheme 1, oHA was obtained by oxidation of hyaluronic acid in the presence of sodium periodate ($NaIO_4$). CuS–BSA nanoparticles and mupirocin were mixed with ADH solution, and C/M@Gel was synthesized by crosslinking the mixed ADH solution with oHA solution. In vitro results showed that the antibacterial effect of C/M@Gel applied with LT–PTT with mupirocin concentration of 0.125 ppm was almost 100%, which was consistent with the result observed in M@Gel with mupirocin concentration of 8 ppm. The combination of LT–PTT with antibiotic therapy greatly enhanced the antibacterial efficacy and reduced the applied dosage of antibiotics. The synergistic antibacterial platform was further applied in treating *MRSA*–infected skin abscess, and the in vivo results showed that the local application of C/M@Gel with NIR irradiation exhibited an excellent treatment efficacy. In vitro and in vivo safety tests also verified that the synergistic antibacterial platform was unharmful to red blood cells (RBCs), surrounding tissues, and main visceral organs, showing good biocompatibility. Overall, the designed synergistic strategy holds great promise to provide a potential solution to slow down the occurrence of antimicrobial resistance.

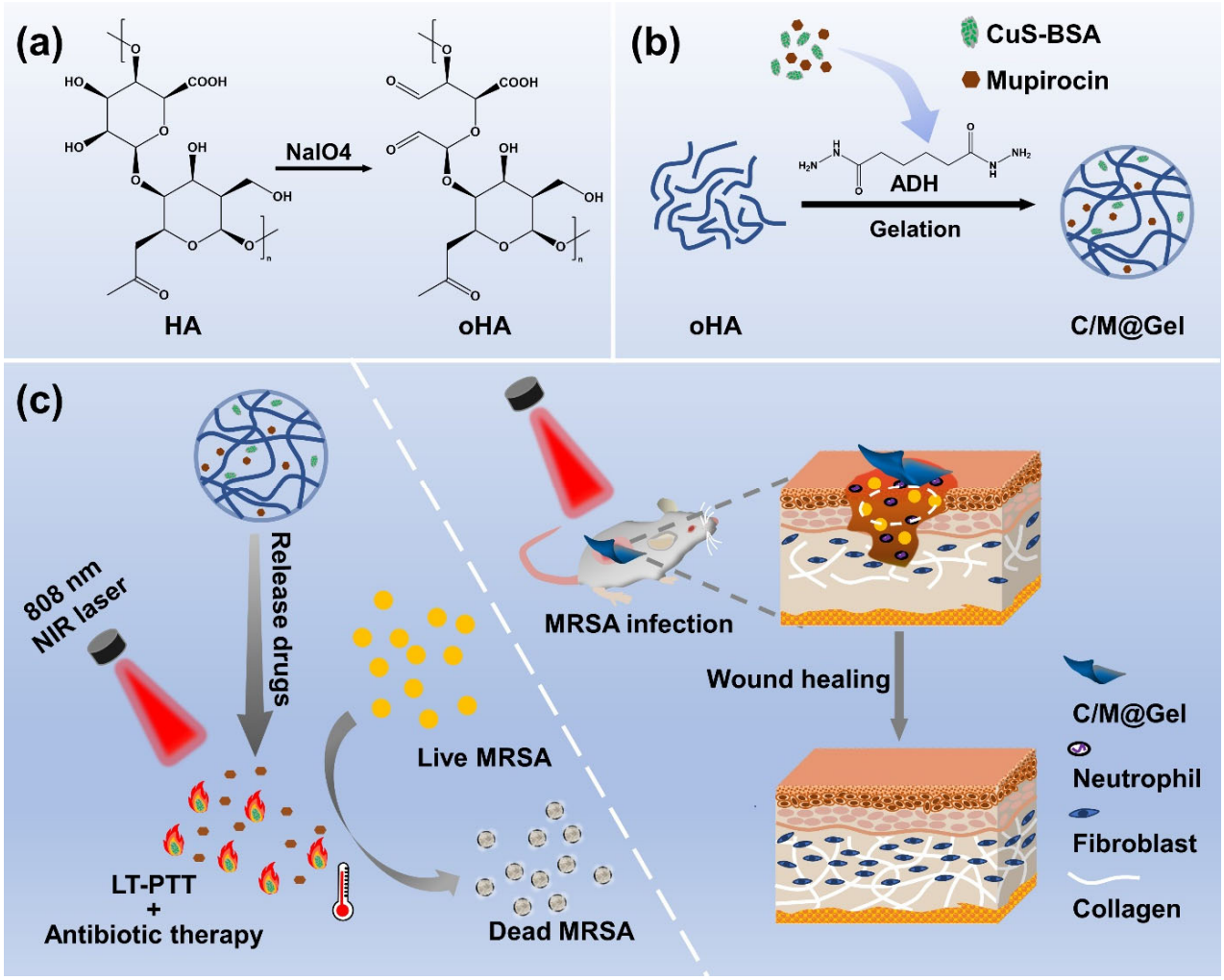

Scheme 1. Schematic illustration of C/M@Gel with NIR irradiation for synergistic therapy. (**a**) Chemical reaction for the synthesis of oHA. (**b**) Preparation process of C/M@Gel. (**c**) Synergistic antibacterial effect of C/M@Gel with NIR irradiation in vitro and in vivo.

2. Materials and Methods

2.1. Materials

Hyaluronic acid (HA, MW = 800,000–1,500,000), sodium periodate ($NaIO_4$), adipic acid dihydrazide (ADH), copper (II) chloride dihydrate ($CuCl_2{\cdot}2H_2O$), tribromoethanol, and sodium sulfide nonahydrate ($Na_2S{\cdot}9H_2O$) were purchased from Macklin (Shanghai, China). Mupirocin was purchased from Yuanye (Shanghai, China), and bovine serum albumin (BSA, MW = 68,000) was purchased from BioFroxx GmbH (Essen, Germany). Ethylene glycol was purchased from Lingfeng (Shanghai, China), and sodium hydroxide (NaOH) was purchased from Xilong (Shantou, China). 3–(4,5–dimethylthiazolyl)–2,5–diphenyltetrazolium bromide (MTT) was purchased from Sigma Aldrich (Shanghai, China). Luria–Bertani (LB) broth and LB agar were purchased from Land Bridge (Beijing, China). Human embryonic kidney cell line HEK–293T was purchased from ATCC (Beijing, China). Methicillin resistant *Staphylococcus aureus* (*MRSA*, ATCC 700788) was kindly provided by Key Laboratory of Tumorigenesis and Intervention in Jiangsu Province, China.

2.2. Synthesis and Characterizations of CuS–BSA

The hydrophilic CuS–BSA nanoparticles were prepared by employing BSA as a template and reducing agent. $CuCl_2{\cdot}2H_2O$ and $Na_2S{\cdot}9H_2O$ served as the copper source and sulfur source, respectively. In a typical procedure, 20 mL of $CuCl_2{\cdot}2H_2O$ solution (1.7 mg/mL)

and 20 mL of BSA solution (10 mg/mL) were prepared and mixed in a round–bottomed flask with magnetic stirring at 800 rpm until the solution turned light green turbidity. Next, NaOH solution (1 mol/L) was added to adjust the mixture to pH 12, and the color turned into transparent dark purple. Subsequently, 400 μL of $Na_2S{\cdot}9H_2O$ (242.16 mg/mL) was quickly added and the solution became dark brown. After stirring for 4 h, the solution was dialyzed (MWCO = 3500 Da) against deionized water for 24 h. Upon lyophilization, the final dark green cotton–like product was collected and stored at 4 °C. For further use, the prepared product CuS–BSA nanoparticles was re–dissolved in PBS (pH = 7.4). The exact concentration of Cu was measured by NexION 2000 inductively coupled plasma–mass spectrometry (ICP–MS, PerkinElmer, Waltham, MA, USA). The morphology of CuS–BSA nanoparticles was observed by HT7700 transmission electron microscope (TEM, Hitachi, Tokyo, Japan). Fourier transform infrared (FT–IR) spectrum of CuS–BSA was measured ranging from 4000 to 400 cm^{-1} using Vertex 70v (Bruker, Billerica, MA, USA). The UV–Vis–NIR absorbance spectrum of synthesized CuS–BSA nanoparticles was measured within the wavelength range of 1360–400 nm by UV–3600 Plus (Shimadzu, Kyoto, Japan). The crystal structure of CuS–BSA nanoparticles was tested with ARL EQUINOX 100 (ThermoFisher, Waltham, MA, USA). The hydrodynamic diameter and zeta potential of CuS–BSA were determined by Zetasizer Nano ZS90 (Malvern, Worcs, UK).

2.3. Photothermal Property of CuS–BSA Nanoparticles

In order to evaluate the photothermal property of CuS–BSA nanoparticles, 200 μL of CuS–BSA solution with different Cu concentrations (0, 6, 12, 24, 48 and 96 ppm, respectively) were first exposed to an 808 nm NIR laser at 0.8 W/cm^2 for 5 min. Next, 200 μL of CuS–BSA solution with Cu concentration of 24 ppm was exposed to an 808 nm NIR laser at different power densities (0.4, 0.6, 0.8, and 1.0 W/cm^2, respectively) for 5 min. Meanwhile, in order to further evaluate the photostability of CuS–BSA nanoparticles, repeated heat/cool cycles were performed. About 200 μL of CuS–BSA aqueous solution with Cu concentration of 24 ppm was irradiated with an 808 nm NIR laser at 0.8 W/cm^2 for 5 min and followed by a 5–min cooling period. This procedure was repeated five times. All the temperature data points were recorded every 20 s using an infrared thermal camera.

2.4. Synthesis and Characterizations of oHA and Gel

For the synthesis of oHA, 1.14 g of HA was dissolved in 120 mL of deionized water with continuous magnetic stirring at 800 rpm. Next, 5 mL of $NaIO_4$ (130 mg/mL) solution was added as an oxidant. After 24 h, The reaction was terminated by adding 5 mL of ethylene glycol and stirring for another 2 h. The mixture was dialyzed (MWCO = 8000–14,000 Da) against deionized water for 3 days to remove excess $NaIO_4$ and ethylene glycol. Upon lyophilization, the final white cotton–like powder was collected and stored at 4 °C. For further use, the prepared oHA was re–dissolved in PBS (pH 7.4). FT–IR spectrum of oHA, ADH and Gel was measured ranging from 4000 to 400 cm^{-1} using Vertex 70v. The molecular structure of oHA was determined by 300 UltraShield ^{1}H NMR Measurement (Bruker, San Jose, CA, USA).

To obtain the appropriate preparation parameters of Gel for the next application, the Gels were prepared by crosslinking 60 mg/mL oHA with different concentrations of ADH (20, 40, and 60 mg/mL, respectively) at a volume ratio of 4:1. Then, the Gels were formed by allowing to stand for 2–5 min at room temperature, and then cut into a cube shape with 10 mm side length. Subsequently, the Gels were subjected to a static compressive test at a compressive rate of 1 mm/min with a TH–8203S tensile testing machine (Tophung, Suzhou, China). The microstructures of Gel were observed by Verios 5 XHR scanning electron microscope (SEM, Thermos, Waltham, MA, USA).

In order to load CuS–BSA nanoparticles and mupirocin into the Gel, CuS–BSA nanoparticles and mupirocin powders were first mixed with 40 mg/mL of ADH solution, respectively. Other experimental procedures were the same as above. Then M@Gel with

mupirocin concentration of 0.125 ppm, C@Gel with Cu concentration of 24 ppm, C/M@Gel with mupirocin concentration of 0.125 ppm and Cu concentration of 24 ppm were obtained.

2.5. Releasing Kinetics of M@Gel and C@Gel

In order to explore the releasing behavior of M@Gel, 1.0 mL of M@Gel with mupirocin concentration of 1.0 mg/mL was prepared in situ in the vial. With the addition of 3 mL PBS buffer (pH 7.4) as releasing medium, the vial was incubated in a shaking bath at 37 °C and shaken at 60 rpm. At scheduled time intervals (3, 6, 9, 12, 18, and 24 h), 300 μL of the releasing medium was collected for sampling and immediately replenished with the same volume of fresh PBS. The collected samples were analyzed by high–performance liquid chromatography (HPLC, Shimadzu, Japan) to assay the amount of the released mupirocin [24]. The HPLC measurements were performed using a reversed–phase C_{18} column (250 mm × 4.6 mm, 5 μm) at 30 °C. The mobile phase consisted of 0.1 mol/L phosphate buffer (pH 6.3) and acetonitrile in the volume ratio 75:25. The injection volume was 20 μL, with a flow rate of 1.0 mL/min. An ultraviolet (UV) detector was set to monitor the wavelength at 230 nm. Three parallels were set for each group. The amount of mupirocin released was calculated and the cumulative release curve was plotted.

Next, C@Gel with CuS–BSA concentration of 0.8 mg/mL was prepared to explore its releasing behavior. And the subsequent procedures were conducted consistent with that of M@Gel. After sample collection, the samples were analyzed with a BCA protein assay kit, and the concentration of BSA in CuS–BSA was measured to indicate the amount of CuS–BSA released. A microplate reader (Tecan, Meilun, Zurich, Switzerland) was used to determine the absorbance value at 540 nm. Three parallels were set for each group.

2.6. In Vitro Cytotoxicity of CuS–BSA

The cytotoxicity of CuS–BSA was evaluated by measuring the viability of 293T cells (human embryonic kidney cell line) with MTT reagent–based colorimetry. In brief, cells in 96–well plates with a density of 10^4 cells/well were incubated with 100 μL DMEM overnight. Next, cells were co–cultured with different concentrations of CuS–BSA solution (Cu concentration: 0, 4, 8, 16, 24, 32, 40, and 48 ppm, respectively). After incubating for 12 h, culture medium was discarded and 100 μL MTT reagent was added instead. Then, the system was cultured at 37 °C for 3 h. After adding 200 μL dimethyl sulfoxide for dissolving the formed formazan crystals, the color intensity was measured at 490 nm using a microplate reader. Each set of data was from three replicates. The percentage of viable cells was calculated with the following formula:

$$\text{Cell Viability } (\%) = \frac{A_{\text{sample}} - A_{\text{MTT}}}{A_{\text{control}} - A_{\text{MTT}}} \times 100$$

where A_{sample} was the absorbance of CuS–BSA groups, A_{MTT} was the absorbance of MTT group, A_{control} was the absorbance of blank group with DMEM only.

2.7. Hemolysis Assay of CuS–BSA and C/M@Gel

According to the reported method with slight modification [25], hemolysis assay was performed to evaluate the compatibility of CuS–BSA and C/M@Gel with RBCs. Previously, different concentrations of CuS–BSA solution (Cu concentration: 12, 24, and 48 ppm) and C/M@Gel with mupirocin concentration of 0.125 ppm and Cu concentration of 24 ppm were prepared and equilibrated in saline for 30 min at 37 °C. RBCs were isolated from fresh mouse blood by centrifugation at 1500 rpm for 1 min. Next, the precipitation was resuspended in saline to form 2% RBCs suspension. About 500 μL of RBCs suspension was mixed with 50 μL of CuS–BSA solution or C/M@Gel, following an incubation for 3 h at 37 °C. The optical density of the supernatant was measured at 540 nm with a microplate reader. Positive and negative controls were set as 50 μL of deionized water and saline,

respectively. Each group was repeated for three times and the hemolysis rate was calculated with the following formula:

$$\text{Hemolysis } (\%) = \frac{A_{\text{sample}} - A_{\text{saline}}}{A_{\text{DI water}} - A_{\text{saline}}} \times 100$$

where A_{sample} was the absorbance of experimental group, A_{saline} was the absorbance of saline group, and $A_{\text{DI water}}$ was the absorbance of deionized water group.

2.8. In Vitro Antibacterial Evaluation

MRSA (Gram–positive) were cultured in sterile liquid LB medium overnight at 37 °C and further diluted with liquid LB medium (1:50) for 3 h to obtain bacteria in logarithmic growth period. The optical density (OD) value at 600 nm was examined to represent the concentration of bacteria. *MRSA* suspension was prepared at a concentration of ca. 1.0×10^7 CFU/mL for further use.

For the in vitro antibacterial assay of monotherapy by LT–PTT or antibiotic therapy, standard plate counting method was applied. Previously, 40 μL of M@Gel containing different concentrations of mupirocin (0, 0.125, 0.5, 2, and 8 ppm, respectively) and 40 μL of C@Gel containing different concentrations of CuS–BSA (Cu concentration: 0, 12, 24, and 48 ppm, respectively) were directly formed in a tube and equilibrated in saline for 30 min at 37 °C, respectively. The appropriate concentrations of CuS–BSA and mupirocin in Gel for synergistic antibacterial therapy were determined by incubation of M@Gel or C@Gel with 160 μL *MRSA* suspension for 24 h at 37 °C, respectively. It should be mentioned that after 12 h of co–incubation, an NIR laser was applied and kept irradiating for 5 min in each C@Gel group.

For the in vitro evaluation of synergistic antibacterial efficacy, the experiment was divided into five groups: G1: PBS, G2: Gel, G3: C@Gel with NIR, G4: M@Gel, G5: C/M@Gel with NIR. The final Cu concentration in both C@Gel and C/M@Gel was 24 ppm, and the final mupirocin concentration in both M@Gel and C/M@Gel was 0.125 ppm. All the groups were incubated with *MRSA* suspension for 24 h at 37 °C, respectively. After 12 h of co–incubation, the C@Gel with NIR and C/M@Gel with NIR groups were irradiated by an NIR laser for 5 min, respectively. After the incubation, all the bacteria in each tube were diluted and 100 μL of each diluent was spread onto LB agar plates to determine the bacterial colonies.

2.9. In Vivo Antibacterial and Wound Healing Effects

The in vivo therapeutic effect of synergistic antibacterial platform was evaluated in a mouse model. Balb/c female mice (7–8 weeks, 18–22 g) were purchased from Qinglongshan animal breeding farm (Henan, China). In vivo anti–infective evaluation was executed under the supervision of the Pharmaceutical Animal Experiment Center of China Pharmaceutical University.

All mice were acclimatized for 1 week before surgery. In order to construct the bacteria–infected mice model, the mice were anesthetized by tribromoethanol, and a full–thickness skin circular wound with a diameter of 7 mm was created on the dorsal area. About 10 μL of *MRSA* suspension (10^8 CFU/mL) was applied to the wound site. After being infected for 24 h, an infected wound model was constructed successfully verified by standard plate counting.

All mice were randomly divided into five groups, and then received different treatments: G1: PBS, G2: Gel, G3: C@Gel with NIR, G4: M@Gel, G5: C/M@Gel with NIR. The Cu concentration in Gel was 24 ppm, and the mupirocin concentration in Gel was 0.125 ppm. All hydrogels were sterilized with UV light for 2 h prior to the experiment. About 400 μL of the hydrogels were applied to the wound surface and renewed every day for four days. For NIR groups, the Gel on the mice wound sites were irradiated with an 808 nm laser (0.8 W/cm^2) for 5 min after 12 h of administration per day, respectively. The temperature changes of the infected sites were recorded by an infrared thermal camera. To

assess the bacterial burden in the wound, the tissue fluid at the wound was dipped and diluted with saline at the end of administration, following the diluent spread on LB plate. After 16 h of incubation, the number of bacterial colonies on each plate was calculated. Body weight and infected area were recorded every day along 10 days of observation. And then all mice were sacrificed and the infected tissues were harvested for hematoxylin and eosin (H&E) and Masson staining. The major organs (heart, liver, spleen, lung, and kidney) were also harvested for H&E staining. Animal experiments were performed in accordance with Institutional Animal Care and Use Committee and approved by the Ethics Committee of China Pharmaceutical University.

2.10. Statistical Analysis

All means were calculated from at least three independent experiments. To compare the significant difference of each group, Student's *t*–test was applied. The results were considered significant if $p < 0.01$ (***).

3. Results

3.1. Synthesis and Characterizations of CuS–BSA

CuS–BSA was synthesized by reacting $CuCl_2$ with Na_2S in the presence of BSA, which played as a template due to its abundant interactive groups [26–28]. TEM image of CuS–BSA nanoparticles exhibited a relatively monodispersed distribution with an average diameter of 10 nm (Figure 1a). As shown in Figure S1b, the averaged hydrodynamic diameter of CuS–BSA nanoparticles in PBS was 47.7 nm, and the zeta potential of CuS–BSA was –21.1 mV. X–ray diffraction (XRD) pattern of CuS–BSA (Figure 1b) displayed a broad peak, suggesting CuS–BSA was in an amorphous state [29]. In FT–IR spectrometry, the intense broad absorption band at 3300 cm^{-1} could be assigned to the stretching vibration of O–H and N–H bands, and the characteristic peaks at 1390 cm^{-1} and 1113 cm^{-1} represented the stretching vibration of [COO–] and C–O–C, respectively [26,30]. The bands located at 1528 cm^{-1} and 1234 cm^{-1} were attributed to amide II and –CO–NH– groups, respectively [26,31] (Figure 1c). All the characteristic peaks of BSA were contained in CuS–BSA, indicating the existence of BSA in CuS–BSA [32]. Moreover, new absorption peak at 621 cm^{-1} attributed to the unique Cu–S tensile vibration appeared, further verifying the successful synthesis of CuS–BSA nanoparticles [30,31]. From the UV–Vis–NIR absorption spectra, CuS–BSA exhibited a strong absorption in a wide NIR range from 780–1200 nm (Figure 1d), which was a good therapeutic window for LT–PTT [33,34].

3.2. Photothermal Property of CuS–BSA

The photothermal performance of CuS–BSA was systematically evaluated in the presence of NIR laser. As presented in Figure 2a, the temperature of the CuS–BSA solution after NIR irradiation kept increasing along with the irradiation time, and the final temperature was positively dependent on the concentration of CuS–BSA. When the Cu concentration in CuS–BSA was 24 ppm, the temperature increased by 17.8 °C upon NIR laser irradiation for 5 min, which was enough for LT–PTT whose temperature was maintained at 45 °C [35]. The photothermal effect of CuS–BSA was also positively correlated with the power density of NIR laser as shown in Figure 2b. When the power density of NIR laser increased from 0.4 to 1.0 W/cm^2, the temperature increased from 7.9 to 21.4 °C. These results showed that CuS–BSA could efficiently convert laser energy into heat via light absorption at 808 nm [36]. As shown in Figure 2c, there was no significant difference in temperature elevation over five irradiation cycles, suggesting that the CuS–BSA possessed excellent photothermal stability. Finally, we measured the photothermal conversion efficiency (η) of CuS–BSA according to the previously reported method. As presented in Figure 2d, the value of η was 39.32%, which demonstrated high ability to transform NIR light into heat and could serve as a potential photothermal agent [37].

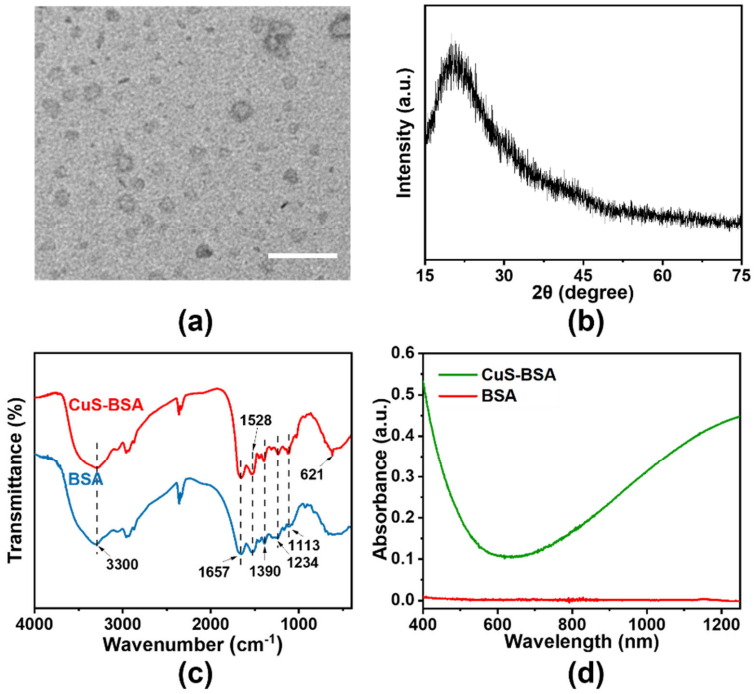

Figure 1. Characterizations of CuS–BSA. (**a**) TEM image of CuS–BSA. Scale bar: 50 nm. (**b**) XRD pattern of CuS–BSA. (**c**) FT–IR spectroscopy of CuS–BSA and BSA. (**d**) UV–Vis–NIR absorbance spectra of CuS–BSA and BSA.

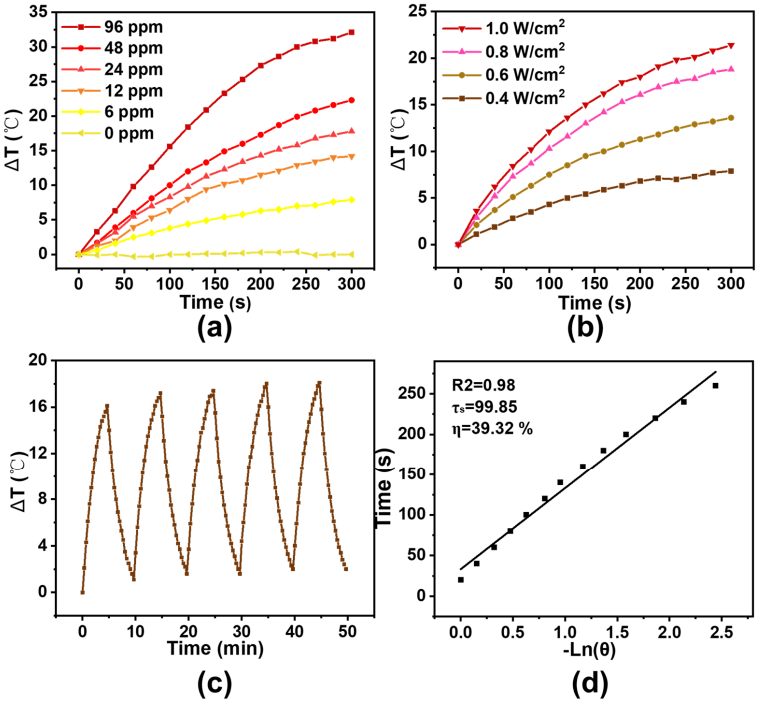

Figure 2. Photothermal conversion efficiency and photothermal stability of CuS–BSA. (**a**) Relative temperature profiles of CuS–BSA with different Cu concentrations (0, 6, 12, 24, 48, 96 ppm) under NIR laser at 0.8 W/cm^2 for 5 min. (**b**) Relative temperature profiles of CuS–BSA with 24 ppm of Cu at different power density (0.4, 0.6, 0.8, 1.0 W/cm^2) for 5 min. (**c**) Temperature curve of 0.8 W/cm^2 laser irradiation on/off cycles of CuS–BSA with 24 ppm of Cu. (**d**) Calculation of the photothermal–conversion efficiency (η) of CuS–BSA under an 808 nm laser.

3.3. Preparation and Characterizations of Gel

The schematic representation of oxidation of HA and crosslink of oHA with ADH is shown in Scheme 1. HA oxidation performed by $NaIO_4$ occurred by cleaving the structure of o–diol and forming aldehyde groups [38]. ^{1}H–NMR spectrum showed a characteristic peak of oHA at 4.9–5.0 ppm, which was corresponding to the aldehyde group and indicated the oxidation of HA [39] (Figures 3a and S2). In FT–IR spectroscopy, a new characteristic peak at 1730 cm^{-1} attributed to the aldehyde group, further demonstrating the successful synthesis of oHA (Figure 3b). However, since some aldehyde groups existed in the form of hemiacetal and aldehyde hydrate, this new absorption peak appeared weakly [40]. According to the previous reported method, based on the results of linear regression (Figure S3) and the measured fluorescence intensity of oHA at 60 mg/mL, we calculated that the aldehyde degree of oHA was 54.88% [41].

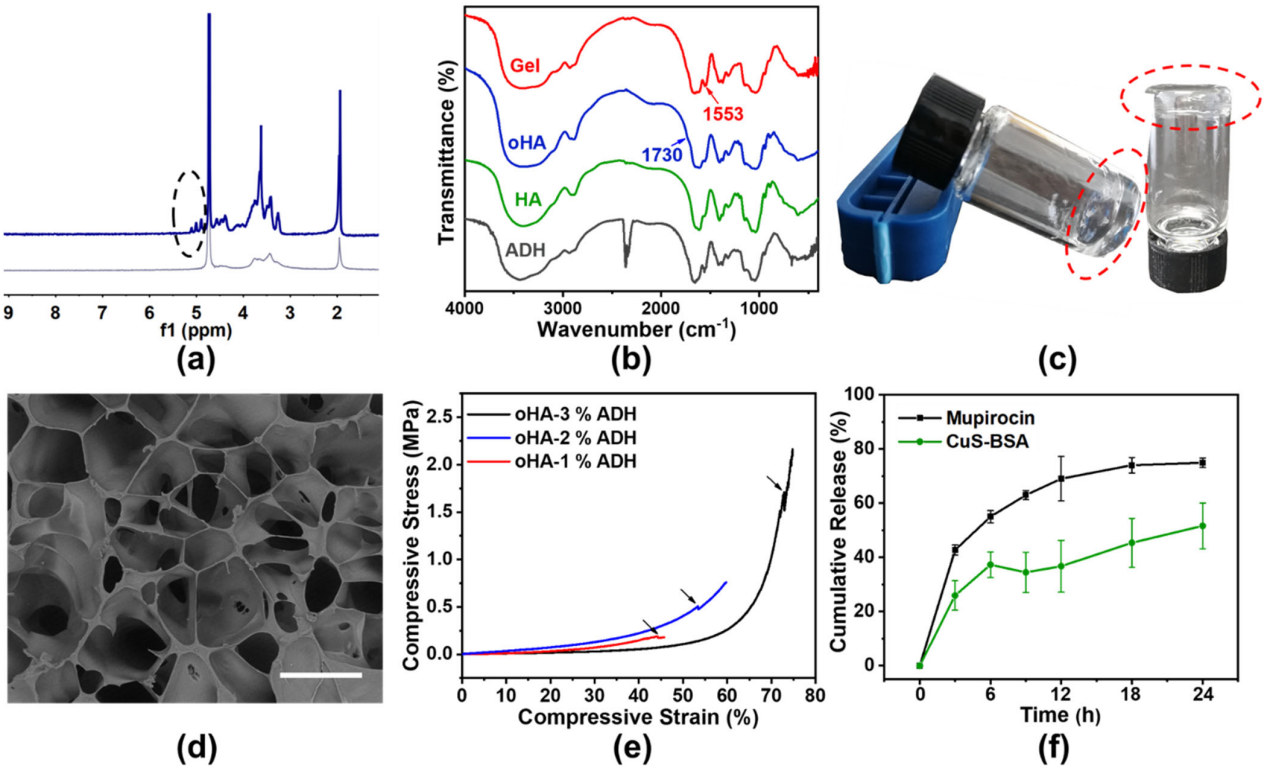

Figure 3. Characterizations of oHA and Gel. (**a**) ^{1}H–NMR spectra of oHA and HA. (**b**) FT–IR spectroscopy of Gel, oHA, ADH, and HA. (**c**) Optical image and (**d**) SEM image of Gel after complete gelation. Scale bar: 100 μm. (**e**) Mechanical properties of Gel with different ADH concentrations (1%, 2%, 3%). (**f**) Release behaviors of M@Gel with mupirocin concentration of 1.0 mg/mL and C@Gel with Cu concentration of 24 ppm.

Biodegradable Gel with three–dimensional network was successfully synthesized by grafting ADH onto the aldehyde group of oHA [22]. After ADH solution was added dropwise to the oHA solution, the crosslinking procedure occurred immediately, and the Gel was formed just in a few minutes (Figure 3c). In FT–IR spectroscopy, the enhanced characteristic peak at 1553 cm^{-1} represented the formation of acyl hydrazone bond [42], the new peak within the fingerprint region from 700–400 cm^{-1} and the disappeared peak at 2360 cm^{-1} of ADH also proved the formation of Gel (Figure 3b). The gelation process was achieved by the formation of acyl hydrazone bond, as the aldehyde moiety with positively charged carbon was vulnerable to nucleophilic attack from hydrazide bonds of ADH [43]. When ADH was at a concentration of 2%, SEM images in Figure 3d showed a cellular network structure of Gel. Rheological experiments were further conducted to study the mechanical properties of Gel with an ADH concentration of 2%. Amplitude

scanning at room temperature and frequency scanning at 4 °C and 45 °C (Figure S4) showed that the hydrogels have good mechanical properties and viscoelastic properties [19]. The crosslinked hydrogel had an available mechanical property and ideal porosity for further use (Figures 3e and S5).

Moreover, the releasing kinetics of M@Gel containing 1.0 mg/mL mupirocin and C@Gel containing 24 ppm Cu were studied. According to the standard curves as shown in Figure S6, the concentration of released mupirocin was detected by HPLC, and the concentration of released CuS–BSA was examined by a BCA protein assay kit. After 24 h, the cumulative release rate of C@Gel and M@Gel were 51.6% and 74.9%, respectively (Figure 3f). The results showed that Gel had excellent drug releasing capacity and could prolong the effective time of drugs.

3.4. Biocompatibility of CuS–BSA and Gel

To investigate the cytotoxicity of CuS–BSA, MTT assay was carried out with 293T cells. Specifically, CuS–BSA with Cu concentration up to 48 ppm did not exhibit any significant toxicity to 293T cells (Figure S7a), which was well above the applied dose (Cu concentration: 24 ppm) for LT–PTT in this study. The results showed that CuS–BSA was unharmful to the surrounding healthy cells, which might be because the negative zeta potential of CuS–BSA (Figure S1a) could lead to reduced unspecific binding with the cellular membranes [44].

The hemolytic test was carried out to investigate the biocompatibility of CuS–BSA and C/M@Gel with mouse RBCs. The OD values at a wavelength of 540 nm were measured for the lysis of mouse RBCs, and the corresponding hemolysis rates are shown in Figure S7b,c. It could be seen that the hemolysis rates were lower than 5% in each group, which were within the permissible range of biomaterials [45]. Therefore, CuS–BSA and the Gel had good blood compatibility and reached the requirements of security for biological applications.

3.5. In Vitro Evaluation of Synergistic Antibacterial Effects

Encouraged by the excellent photothermal ability of CuS–BSA and good biocompatibility of C/M@Gel, the synergistic antibacterial potential against *MRSA* was evaluated. First, the antibacterial efficiency of different groups of M@Gel was evaluated and the concentrations of mupirocin in Gel was 0.125, 0.5, 2, and 8 ppm, respectively. As shown in Figure 4a, the Gel group showed a slight lethal effect, which might be due to the adhesion of bacteria by Gel. The amounts of bacteria in M@Gel groups decreased as the concentration of mupirocin increased. The quantitative representation of antibacterial efficacy in M@Gel groups was shown in Figure 4b. The results showed that 56.5% of the bacteria could survive after the treatment of M@Gel with mupirocin concentration of 0.125 ppm. Particularly, the antibacterial rate of M@Gel with mupirocin concentration of 8 ppm was up to 100%, suggesting that the growth of bacteria could be inhibited efficiently under a relatively high mupirocin concentration.

Meanwhile, the antibacterial performance of C@Gel was conducted with NIR laser irradiation for 5 min after 12 h of treatment. Different groups of C@Gel (Cu concentration: 12, 24 and 48 ppm, respectively) were incubated with *MRSA* for 24 h. As shown in Figure S9, all C@Gel groups showed slight influence on the survival of bacteria, demonstrating the monotherapy of LT–PTT by C@Gel was not sufficient for antibacterial treatment. In order to evaluate the antibacterial effect by LT–PTT of CuS–BSA nanoparticles, we compared the bacterial viability in C@Gel group with or without NIR irradiation. As shown in Figure S8a, the bacteria viability was 90.5% after incubated with C@Gel for 24 h, while the survival percentage of bacteria was 88.6% after applying NIR irradiation for 5 min along the above treatment. The results demonstrated that LT–PTT of CuS–BSA NPs only showed slight antibacterial effect against *MRSA*.

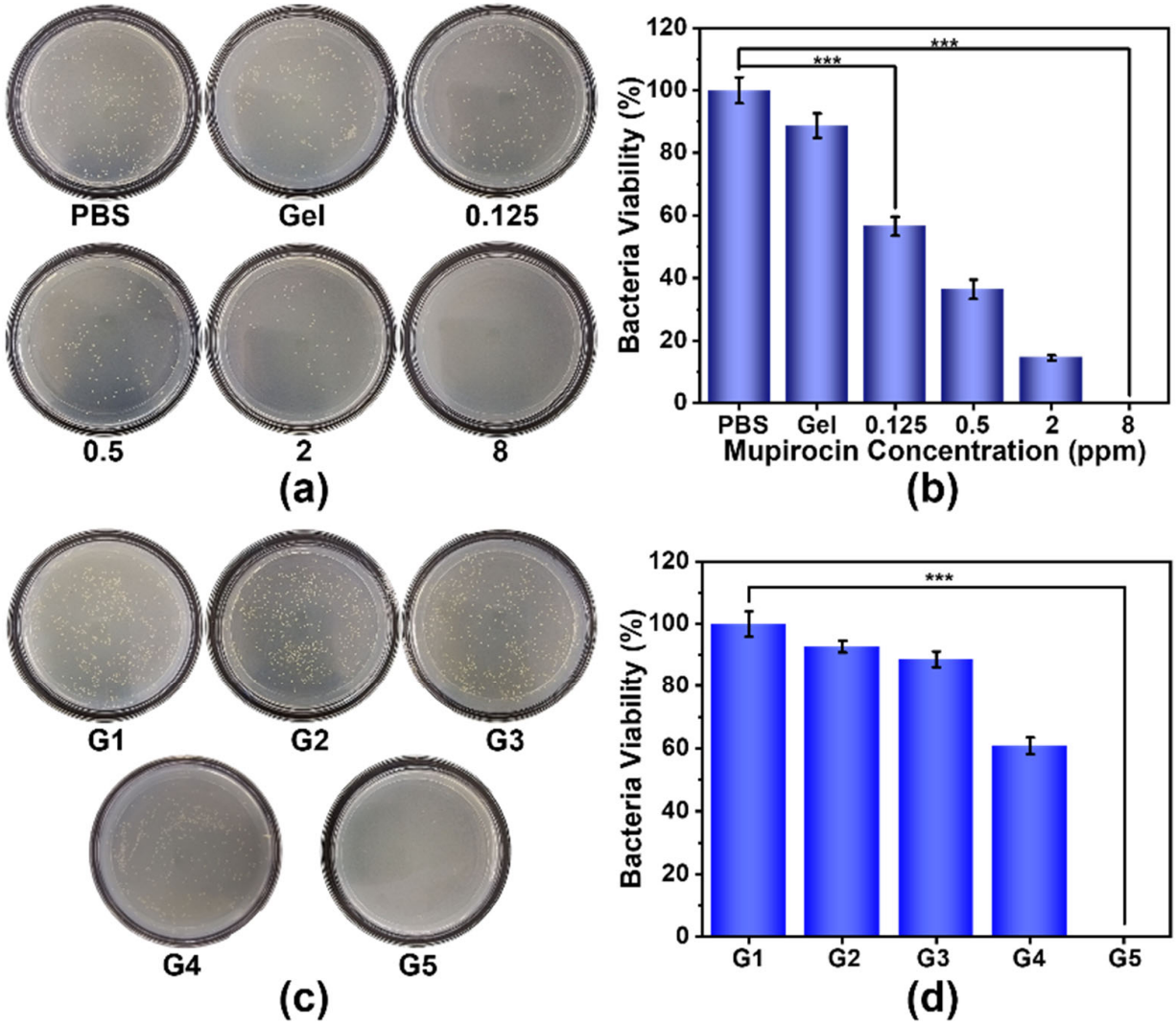

Figure 4. Antibacterial evaluation of mono/synergistic therapy in vitro. Results of (**a**) standard plate counting and (**b**) survival percentages of *MRSA* after 24 h of incubation with PBS, Gel, and M@Gels with mupirocin concentrations of 0.125, 0.5, 2, and 8 ppm, respectively. Results of (**c**) standard plate counting and (**d**) survival percentages of *MRSA* after 24 h of mono/synergistic treatments. G1: PBS, G2: Gel, G3: C@Gel with NIR, G4: M@Gel, G5: C/M@Gel with NIR. Mupirocin concentration in M@Gel and C/M@Gel: 0.125 ppm, Cu concentration in C@Gel and C/M@Gel: 24 ppm. (Error bar: mean ± SD, *** $p < 0.001$).

In order to further explore the synergistic antibacterial performance of LT–PTT and antibiotic therapy, the in vitro experiment was divided into five groups, including G1: PBS, G2: Gel, G3: C@Gel with NIR, G4: M@Gel, and G5: C/M@Gel with NIR. The Cu concentration in C@Gel and C/M@Gel was 24 ppm, and the mupirocin concentration in M@Gel and C/M@Gel was 0.125 ppm. The results of standard plate counting and quantitative expression were shown in Figure 4c,d, respectively. The bacterial survival rate was 88.7% in G3 (only LT–PTT) and 60.9% in G4 (only antibiotic therapy), indicating that the single bacterial killing effect of LT–PTT or antibiotic therapy could not completely remove *MRSA*. However, when applying NIR irradiation for 5 min, the C/M@Gel with a much lower dose of mupirocin at 0.125 ppm could achieve a superior antibacterial efficacy of almost 100% against *MRSA*. The bacterial viability in C/M@Gel group with or without NIR irradiation were also compared to investigate the practical role of LT–PTT. As shown in Figure S8b, the antibacterial efficiency in C/M@Gel group was 50.9%, while no bacteria colonies were observed after 5 min of NIR irradiation was added. The results demonstrated

that LT–PTT could enhance the antibiotic therapy but not the CuS–BSA NPs itself. The above results illustrated that C/M@Gel with NIR irradiation synergized by LT–PTT and antibiotic therapy could kill bacteria more efficiently under a safe temperature and low dosage.

3.6. In Vivo Assay

Considering the remarkable synergistic antibacterial performance in vitro, female Balb/c mice models infected with *MRSA* were built to estimate the antibacterial potential of the synergistic antibacterial platform C/M@Gel with NIR irradiation in vivo.

Healthy mice were randomly divided into five groups and received different treatments: including G1: PBS, G2: Gel, G3: C@Gel with NIR, G4: M@Gel, G5: C/M@Gel with NIR. The treatment procedure was illustrated in Figure 5a. *MRSA*–infected focal wounds were established in the mice model by adding 20 μL of bacterial suspension (1×10^7 CFU/mL) to the defected dorsal skin and incubating for 24 h. At the first four days, each group received different treatments per day. To evaluate the antibacterial effect of C/M@Gel with NIR irradiation for wound infection, the body fluid around the infected wound was extracted and analyzed by standard plate counting at the end of four days of different treatments. The temperature of the infected wound was examined and exhibited by thermographic images. As seen in Figure 5b, the site of infected wound yielded an elevated temperature maintained at about 45 °C in C/M@Gel with NIR group, while the elevated temperature in PBS group was negligible. As shown in Figures 5c and S10, in the PBS group, the wounds healed slowly due to self–healing ability, but there were still obvious pus and large numbers of bacteria remaining in the wound, which may aggravate the infection. Accelerated wound healing and fewer bacteria could be observed in C@Gel with NIR and M@Gel groups, which was attributed to certain antibacterial effects of CuS–BSA and mupirocin. Remarkably, minimal wound area and complete ablation of bacteria colonies were presented in the C/M@Gel with NIR group, demonstrating that the synergistic platform combining LT–PTT and antibiotic therapy had excellent antibacterial efficacy [14] (Figure 5d,e). These results demonstrated that the established synergistic antibacterial platform C/M@Gel with NIR irradiation possessed an ideal antibacterial effect and could effectively inhibit bacterial survival, and further accelerate wound healing. Meanwhile, the body weight of mice remained stable along the treatment process, which demonstrated bare side effects and good compatibility of C/M@Gel (Figure 5f).

3.7. Histological Analysis

The healing states of treated wounds were assessed by H&E staining and Masson staining. In Figure 6a, H&E staining disclosed that there were obvious signs of tissue infections and skin ulcers in the PBS groups, including many macrophages and neutrophils infiltrating in the tissues. By contrast, the wound was almost completely healed, and the wound tissue was mainly composed of fibrous cells arranging in order in the C/M@Gel with NIR group. Masson staining showed that there was structural disorder of muscle fibers and collagen fibers in PBS group, but there was no obvious destroy in C/M@Gel with NIR group. Meanwhile, as shown in Figure 6b, there was no obvious abnormality in the sections of main visceral tissues (heart, liver, spleen, lung, and kidney) for C/M@Gel with NIR group, indicating that the side effects of this synergistic antibacterial system were negligible in mice.

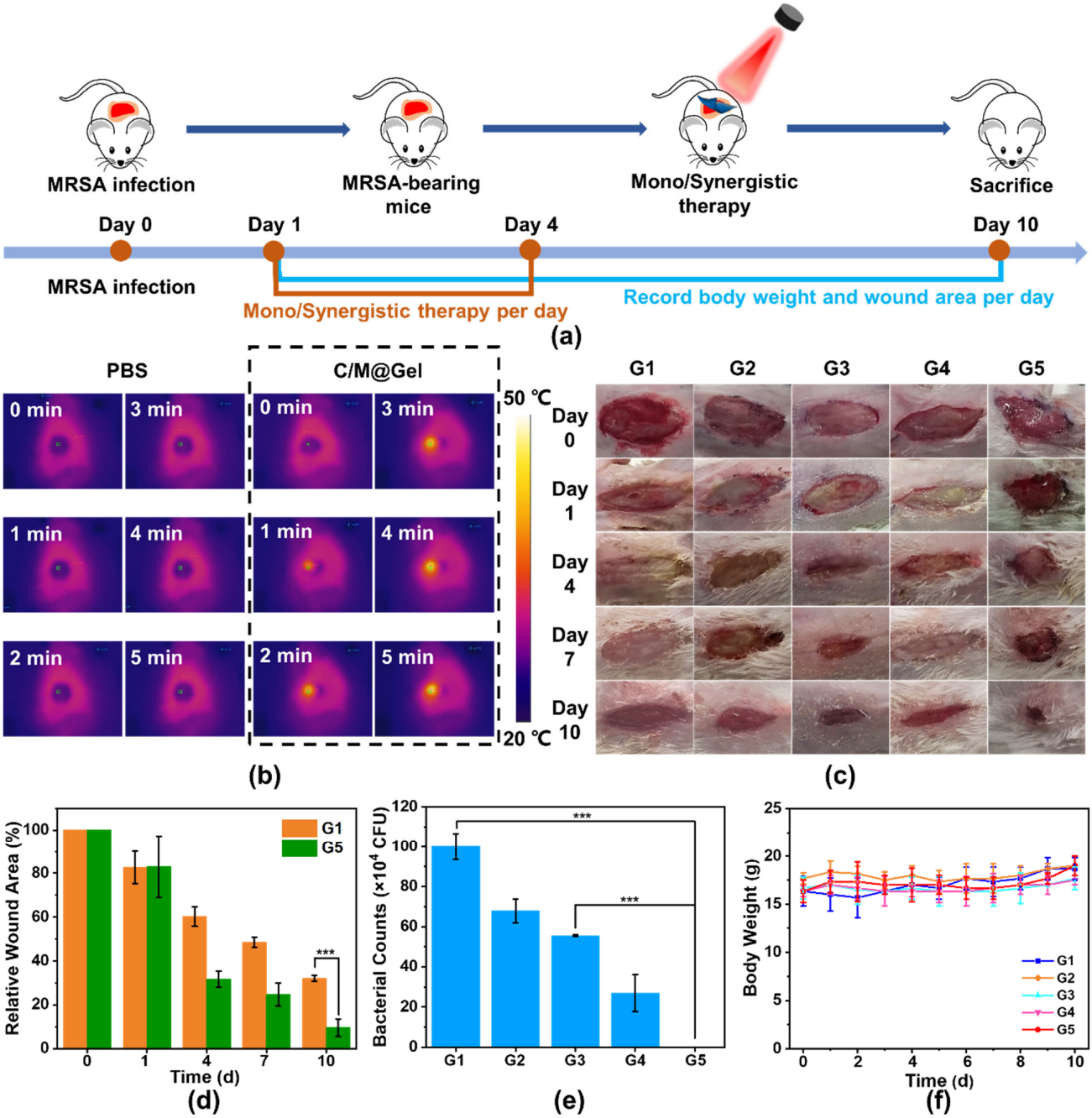

Figure 5. Antibacterial performance of mono/synergistic therapy in vivo. (**a**) Schematic description of the treatment procedure in vivo. (**b**) Temperature elevation of infected area under NIR laser at 0.8 W/cm^2 within 5 min after PBS and C/M@Gel with NIR treatments, respectively. (**c**) Representative images of skin wounds during the treatment process in vivo. (**d**) Quantitative wound areas during the treatment process. (**e**) Quantitative representation of residual bacteria at the wound site after four consecutive days of mono/synergistic therapy. (**f**) Body weight records of mice along different treatment procedures. G1: PBS, G2: Gel, G3: C@Gel with NIR, G4: M@Gel, G5: C/M@Gel with NIR. Mupirocin concentration in M@Gel and C/M@Gel: 0.125 ppm, Cu concentration in C@Gel and C/M@Gel: 24 ppm. (Error bar: mean ± SD, *** $p < 0.001$).

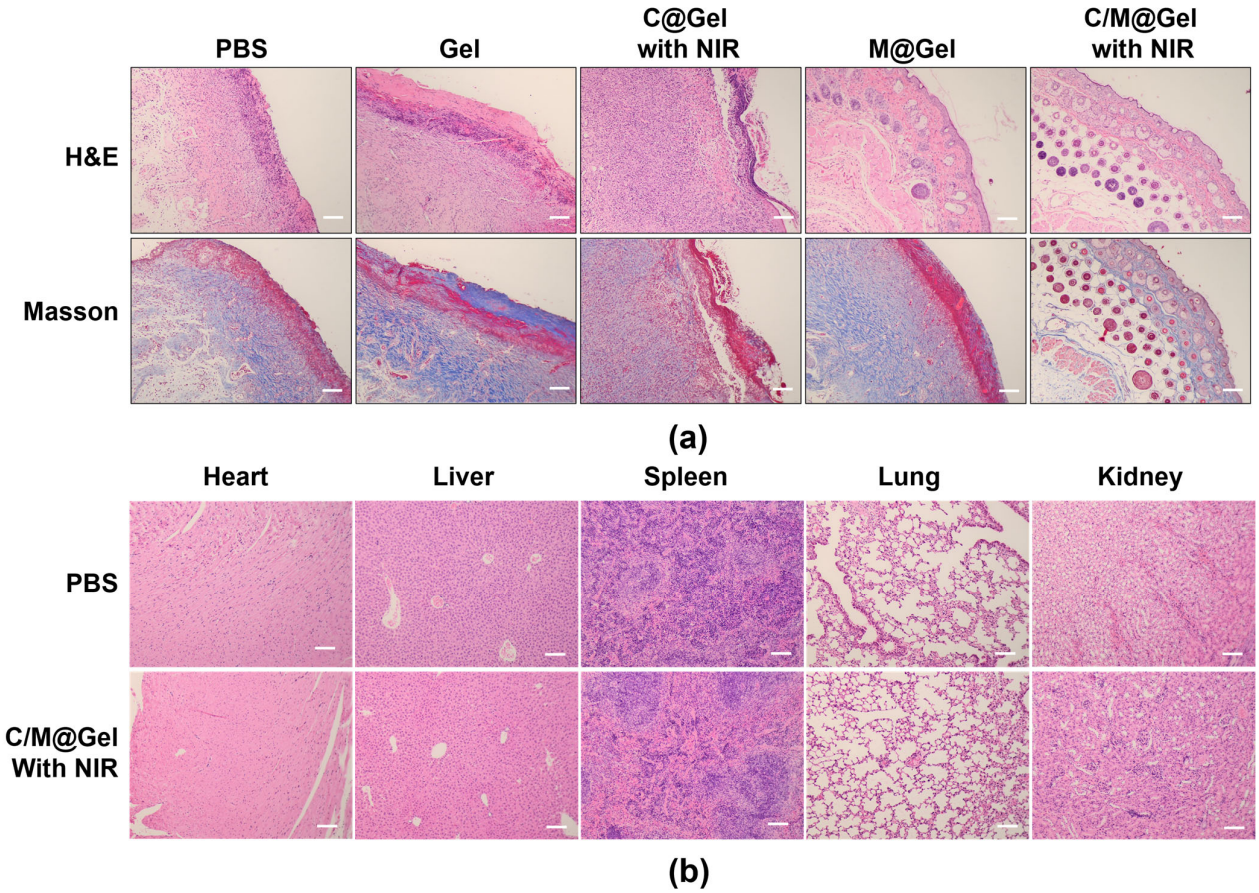

Figure 6. Histological analysis of infected skin and main visceral organs. (**a**) Representative H&E and Masson staining images of the infected skin after different treatments of PBS, Gel, C@Gel with NIR, M@Gel and C/M@Gel with NIR. Scale bars: 100 μm. (**b**) H&E staining of heart, liver, spleen, lung, and kidney after the treatments in PBS and C/M@Gel with NIR group. Scale bars: 100 μm.

4. Discussion

With the occurrence of antimicrobial resistance, bacterial susceptibility to antibiotics decreases, which limits the application of antibiotics in clinical practice. The development of synergetic therapy provides possibility for the reuse of insensitive antibiotics and enlightenment for the treatment strategy of drug–resistant bacteria.

In this study, we evaluated the differences between monotherapy and synergistic therapy in terms of antimicrobial efficiency with standard plate counting methods, to determine the superiority of synergistic therapy. By combining a mouse model with *MRSA*–infected focal wounds, we found that LT–PTT improved the effectiveness of antibiotic therapy, achieving almost 100% bacterial clearance despite a 64–fold reduction of the mupirocin dose compared to the antibiotic therapy only. It was reported that the commercially available mupirocin ointment has been reported to contain 20 mg/g of mupirocin [46]. Therefore, the applied dosage of mupirocin in our synergistic treatment, which was 0.125 ppm, was much less than that of clinical used. Our method could greatly reduce the dosage of antibiotics and thus slow down the occurrence of drug resistance. A previous study demonstrated that photothermal effect could destroy the bacteria cells and membrane, thus improving the drug sensitivity of existing antibiotics and eliminating drug–resistant bacteria [47]. In our work, LT–PTT instead of high–temperature photothermal therapy, as an adjunct treatment, did not exhibit significant antibacterial effect by itself, while it could enhance the sensitivity of bacteria to antibiotics and improve the antibacterial effect of antibiotics. Wu et al. employed proteomic technique and molecular dynamics simu-

lation to verify the LT–PTT as an exogenous–modifying enzyme inhibitor to cooperate aminoglycoside antibiotics against *MRSA* [12]. This report may explain our findings.

The thermal effect could be achieved in deeper tissues by applying magnetic field, ultrasound, or microwave instead of photothermal agents. Meanwhile, since the accumulation of Cu ions of CuS–BSA nanoparticles could do harm to the surrounding healthy tissues, long–term application of CuS–BSA NPs could be avoided and alternative photothermal agents should be developed. There is a long way to fight against antimicrobial resistance and our work still has new points to be improved and further developed.

5. Conclusions

In summary, we developed a synergistic antibacterial strategy combining LT–PTT with antibiotic therapy. The C/M@Gel exhibited an excellent antibacterial effect in vitro. Meanwhile, the cytotoxicity and hemolysis test proved its superior biocompatibility. *MRSA*–infected Balb/c mice models were used to evaluate the antibacterial effects of C/M@Gel in vivo, and the results showed that the combination of CuS–BSA and mupirocin could remove bacteria in infected sites synergistically and accelerate wound healing with minor toxicity. This work provided a synergistic antibacterial platform with improved antibacterial efficacy under relatively low dose of antibiotics and mild temperature. It could propose a new strategy to prolong the effective times of antibiotics and slow down the occurrence of antibiotic resistance.

Supplementary Materials: The following supporting information can be downloaded at: https://www.mdpi.com/article/10.3390/futurepharmacol3010013/s1, Figure S1: Characterization of CuS-BSA; Figure S2: Characterization of oHA and HA; Figure S3: Calculation of aldehyde degree of oHA; Figure S4: Rheological tests of Gel. Figure S5: SEM images of Gel with different ADH concentrations; Figure S6: Standard curve of CuS-BSA and mupirocin; Figure S7: Biocompatibility of CuS-BSA and C/M@Gel; Figure S8: Comparation of bacteria viability in different groups with or without NIR irradiation; Figure S9: Antibacterial efficacy of C@Gel in vitro; Figure S10: Standard plate counting of residual bacteria at the wound site after four consecutive days of mono/synergistic therapy.

Author Contributions: Conceptualization, Q.Z. and Y.J.; methodology, Q.Z., L.C., C.S., C.L., and Y.J.; data curation, Q.Z., Y.J., and S.D.; formal analysis, Q.Z., Y.J., L.C., and P.D.; investigation, Q.Z. and L.C.; writing—original draft preparation, Q.Z.; writing—review and editing, W.Z., S.Z., C.S., and P.W.; supervision, J.D. and Y.J.; funding acquisition, J.D. and Y.J. All authors have read and agreed to the published version of the manuscript.

Funding: This work was partially supported by the Natural Science Foundation of Jiangsu Province (Grant No. BK20200574) and the National Natural Science Foundation of China (Grant No. 52002402, No. 31872479).

Institutional Review Board Statement: All animal procedures were performed in accordance with the Guidelines for Care and Use of Laboratory Animals of China Pharmaceutical University and approved by the Animal Ethics Committee of School of Pharmacy, China Pharmaceutical University.

Informed Consent Statement: Not applicable.

Data Availability Statement: Not applicable.

Acknowledgments: The work was performed using HPLC, UV–Vis and IR on the pharmaceutical analysis teaching platform of China Pharmaceutical University, and the animal experiments were carried out in the animal experiment center of China Pharmaceutical University. We thank Ning Li and Lin Ge for the constructive instructions.

Conflicts of Interest: The authors declare no conflict of interest.

References

1. Ren, Z.; Silverberg, J.I. Burden, risk factors, and infectious complications of cellulitis and erysipelas in US adults and children in the emergency department setting. *J. Am. Acad. Dermatol.* **2021**, *84*, 1496–1503. [CrossRef] [PubMed]
2. Raff, A.B.; Kroshinsky, D. Cellulitis: A Review. *JAMA* **2016**, *316*, 325–337. [CrossRef]
3. Reyes, M.; Filbin, M.R.; Bhattacharyya, R.P.; Billman, K.; Eisenhaure, T.; Hung, D.T.; Levy, B.D.; Baron, R.M.; Blainey, P.C.; Goldberg, M.B.; et al. An immune–cell signature of bacterial sepsis. *Nat. Med.* **2020**, *26*, 333–340. [CrossRef] [PubMed]
4. Zhang, L.; Wang, Y.; Wang, J.; Wang, Y.; Chen, A.; Wang, C.; Mo, W.; Li, Y.; Yuan, Q.; Zhang, Y. Photon–Responsive Antibacterial Nanoplatform for Synergistic Photothermal–/Pharmaco–Therapy of Skin Infection. *ACS Appl. Mater. Interfaces* **2019**, *11*, 300–310. [CrossRef]
5. Murray, C.J.L.; Ikuta, K.S.; Sharara, F. Global burden of bacterial antimicrobial resistance in 2019: A systematic analysis. *Lancet* **2022**, *399*, 629–655. [CrossRef]
6. Zheng, K.; Setyawati, M.I.; Lim, T.P.; Leong, D.T.; Xie, J. Antimicrobial Cluster Bombs: Silver Nanoclusters Packed with Daptomycin. *ACS Nano* **2016**, *10*, 7934–7942. [CrossRef] [PubMed]
7. Lin, X.; Fang, Y.; Hao, Z.; Wu, H.; Zhao, M.; Wang, S.; Liu, Y. Bacteria–Triggered Multifunctional Hydrogel for Localized Chemodynamic and Low–Temperature Photothermal Sterilization. *Small* **2021**, *17*, e2103303. [CrossRef]
8. Ouyang, B.; Liu, F.; Ruan, S.; Liu, Y.; Guo, H.; Cai, Z.; Yu, X.; Pang, Z.; Shen, S. Localized Free Radicals Burst Triggered by NIR–II Light for Augmented Low–Temperature Photothermal Therapy. *ACS Appl. Mater. Interfaces* **2019**, *11*, 38555–38567. [CrossRef]
9. Xu, X.; Liu, X.; Tan, L.; Cui, Z.; Yang, X.; Zhu, S.; Li, Z.; Yuan, X.; Zheng, Y.; Yeung, K.W.K.; et al. Controlled–temperature photothermal and oxidative bacteria killing and acceleration of wound healing by polydopamine–assisted Au–hydroxyapatite nanorods. *Acta Biomater.* **2018**, *77*, 352–364. [CrossRef]
10. Zhu, K.; Qian, S.; Guo, H.; Wang, Q.; Chu, X.; Wang, X.; Lu, S.; Peng, Y.; Guo, Y.; Zhu, Z.; et al. pH–Activatable Organic Nanoparticles for Efficient Low–Temperature Photothermal Therapy of Ocular Bacterial Infection. *ACS Nano* **2022**, *16*, 11136–11151. [CrossRef]
11. Yang, K.; Zhao, S.; Li, B.; Wang, B.; Lan, M.; Song, X. Low temperature photothermal therapy: Advances and perspectives. *Coord. Chem. Rev.* **2022**, *454*, 214330. [CrossRef]
12. Tan, L.; Zhou, Z.; Liu, X.; Li, J.; Zheng, Y.; Cui, Z.; Yang, X.; Liang, Y.; Li, Z.; Feng, X.; et al. Overcoming Multidrug–Resistant *MRSA* Using Conventional Aminoglycoside Antibiotics. *Adv. Sci.* **2020**, *7*, 1902070. [CrossRef] [PubMed]
13. Chen, Q.; Hu, Q.; Dukhovlinova, E.; Chen, G.; Ahn, S.; Wang, C.; Ogunnaike, E.A.; Ligler, F.S.; Dotti, G.; Gu, Z. Photothermal Therapy Promotes Tumor Infiltration and Antitumor Activity of CAR T Cells. *Adv. Mater.* **2019**, *31*, e1900192. [CrossRef] [PubMed]
14. Ma, M.; Liu, X.; Tan, L.; Cui, Z.; Yang, X.; Liang, Y.; Li, Z.; Zheng, Y.; Yeung, K.W.K.; Wu, S. Enhancing the antibacterial efficacy of low–dose gentamicin with 5 minute assistance of photothermy at 50 degrees C. *Biomater. Sci.* **2019**, *7*, 1437–1447. [CrossRef]
15. Qi, C.; Jiang, C.; Fu, L.-H.; Sun, T.; Wang, T.; Lin, J.; Nie, Z.; Huang, P. Melanin–instructed biomimetic synthesis of copper sulfide for cancer phototheranostics. *Chem. Eng. J.* **2020**, *388*, 124232. [CrossRef]
16. Li, L.; Cheng, X.; Huang, Q.; Cheng, Y.; Xiao, J.; Hu, J. Sprayable Antibacterial Hydrogels by Simply Mixing of Aminoglycoside Antibiotics and Cellulose Nanocrystals for the Treatment of Infected Wounds. *Adv. Healthc. Mater.* **2022**, *11*, e2201286. [CrossRef] [PubMed]
17. Li, L.; Scheiger, J.M.; Levkin, P.A. Design and Applications of Photoresponsive Hydrogels. *Adv. Mater.* **2019**, *31*, e1807333. [CrossRef]
18. Yang, K.; Han, Q.; Chen, B.; Zheng, Y.; Zhang, K.; Li, Q.; Wang, J. Antimicrobial hydrogels: Promising materials for medical application. *Int. J. Nanomed.* **2018**, *13*, 2217–2263. [CrossRef]
19. Su, W.Y.; Chen, Y.C.; Lin, F.H. Injectable oxidized hyaluronic acid/adipic acid dihydrazide hydrogel for nucleus pulposus regeneration. *Acta Biomater.* **2010**, *6*, 3044–3055. [CrossRef]
20. Kim, H.S.; Lee, K.Y. Stretchable and self–healable hyaluronate–based hydrogels for three–dimensional bioprinting. *Carbohydr. Polym.* **2022**, *295*, 119846. [CrossRef]
21. Chen, F.; Ni, Y.; Liu, B.; Zhou, T.; Yu, C.; Su, Y.; Zhu, X.; Yu, X.; Zhou, Y. Self–crosslinking and injectable hyaluronic acid/RGD–functionalized pectin hydrogel for cartilage tissue engineering. *Carbohydr. Polym.* **2017**, *166*, 31–44. [CrossRef]
22. Xue, F.; Zhang, H.; Hu, J.; Liu, Y. Hyaluronic acid nanofibers crosslinked with a nontoxic reagent. *Carbohydr. Polym.* **2021**, *259*, 117757. [CrossRef]
23. Liang, H.T.; Lai, X.S.; Wei, M.F.; Lu, S.H.; Wen, W.F.; Kuo, S.H.; Chen, C.M.; Tseng, W.I.; Lin, F.H. Intratumoral injection of thermogelling and sustained–release carboplatin–loaded hydrogel simplifies the administration and remains the synergistic effect with radiotherapy for mice gliomas. *Biomaterials* **2018**, *151*, 38–52. [CrossRef]
24. Liao, C.H.; Chen, C.S.; Chen, Y.C.; Jiang, N.E.; Farn, C.J.; Shen, Y.S.; Hsu, M.L.; Chang, C.H. Vancomycin–loaded oxidized hyaluronic acid and adipic acid dihydrazide hydrogel: Bio–compatibility, drug release, antimicrobial activity, and biofilm model. *J. Microbiol. Immunol. Infect.* **2020**, *53*, 525–531. [CrossRef]
25. Ghorpade, V.S.; Yadav, A.V.; Dias, R.J. Citric acid crosslinked cyclodextrin/hydroxypropylmethylcellulose hydrogel films for hydrophobic drug delivery. *Int. J. Biol. Macromol.* **2016**, *93*, 75–86. [CrossRef]

26. Yang, W.; Guo, W.; Le, W.; Lv, G.; Zhang, F.; Shi, L.; Wang, X.; Wang, J.; Wang, S.; Chang, J.; et al. Albumin–Bioinspired Gd: CuS Nanotheranostic Agent for In Vivo Photoacoustic/Magnetic Resonance Imaging–Guided Tumor–Targeted Photothermal Therapy. *ACS Nano* **2016**, *10*, 10245–10257. [CrossRef]
27. Xiao, Y.; Peng, J.; Liu, Q.; Chen, L.; Shi, K.; Han, R.; Yang, Q.; Zhong, L.; Zha, R.; Qu, Y.; et al. Ultrasmall CuS@BSA nanoparticles with mild photothermal conversion synergistically induce MSCs–differentiated fibroblast and improve skin regeneration. *Theranostics* **2020**, *10*, 1500–1513. [CrossRef]
28. Villanueva, M.E.; Diez, A.M.; Gonzalez, J.A.; Perez, C.J.; Orrego, M.; Piehl, L.; Teves, S.; Copello, G.J. Antimicrobial Activity of Starch Hydrogel Incorporated with Copper Nanoparticles. *ACS Appl. Mater. Interfaces* **2016**, *8*, 16280–16288. [CrossRef] [PubMed]
29. Fu, J.J.; Sun, C.; Tan, Z.F.; Zhang, G.Y.; Chen, G.B.; Song, L. Nanocomplexes of curcumin and glycated bovine serum albumin: The formation mechanism and effect of glycation on their physicochemical properties. *Food Biochem.* **2022**, *368*, 130651. [CrossRef] [PubMed]
30. Mo, S.; Song, Y.; Lin, M.; Wang, J.; Zhang, Z.; Sun, J.; Guo, D.; Liu, L. Near–infrared responsive sulfur vacancy–rich CuS nanosheets for efficient antibacterial activity via synergistic photothermal and photodynamic pathways. *J. Colloid Interface Sci.* **2022**, *608*, 2896–2906. [CrossRef] [PubMed]
31. Huang, G.-Y.; Chang, W.-J.; Lu, T.-W.; Tsai, I.L.; Wu, S.-J.; Ho, M.-H.; Mi, F.-L. Electrospun CuS nanoparticles/chitosan nanofiber composites for visible and near–infrared light–driven catalytic degradation of antibiotic pollutants. *Chem. Eng. J.* **2022**, *431*, 134059. [CrossRef]
32. Wang, D.; Dong, H.; Li, M.; Meng, X.; Cao, Y.; Zhang, K.; Dai, W.; Wang, C.; Zhang, X. Hyaluronic Acid Encapsulated CuS Gel–Mediated Near–Infrared Laser–Induced Controllable Transdermal Drug Delivery for Sustained Therapy. *ACS Sustain. Chem. Eng.* **2017**, *5*, 6786–6794. [CrossRef]
33. Bian, K.; Zhang, X.; Liu, K.; Yin, T.; Liu, H.; Niu, K.; Cao, W.; Gao, D. Peptide–Directed Hierarchical Mineralized Silver Nanocages for Anti–Tumor Photothermal Therapy. *ACS Sustain. Chem. Eng.* **2018**, *6*, 7574–7588. [CrossRef]
34. Deng, G.; Li, S.; Sun, Z.; Li, W.; Zhou, L.; Zhang, J.; Gong, P.; Cai, L. Near–infrared fluorescence imaging in the largely unexplored window of 900–1000 nm. *Theranostics* **2018**, *8*, 4116–4128. [CrossRef]
35. Fan, X.L.; Li, H.Y.; Ye, W.Y.; Zhao, M.Q.; Huang, D.N.; Fang, Y.; Zhou, B.Q.; Ren, K.F.; Ji, J.; Fu, G.S. Magainin–modified polydopamine nanoparticles for photothermal killing of bacteria at low temperature. *Colloids Surf. B* **2019**, *183*, 110423. [CrossRef] [PubMed]
36. Mutalik, C.; Okoro, G.; Krisnawati, D.I.; Jazidie, A.; Rahmawati, E.Q.; Rahayu, D.; Hsu, W.T.; Kuo, T.R. Copper sulfide with morphology–dependent photodynamic and photothermal antibacterial activities. *J. Colloid Interface Sci.* **2022**, *607*, 1825–1835. [CrossRef] [PubMed]
37. Li, J.; Liu, X.; Tan, L.; Cui, Z.; Yang, X.; Liang, Y.; Li, Z.; Zhu, S.; Zheng, Y.; Yeung, K.W.K.; et al. Zinc–doped Prussian blue enhances photothermal clearance of Staphylococcus aureus and promotes tissue repair in infected wounds. *Nat. Commun.* **2019**, *10*, 4490. [CrossRef] [PubMed]
38. França, C.G.; Sacomani, D.P.; Villalva, D.G.; Nascimento, V.F.; Dávila, J.L.; Santana, M.H.A. Structural changes and crosslinking modulated functional properties of oxi–HA/ADH hydrogels useful for regenerative purposes. *Eur. Polym. J.* **2019**, *121*, 109288. [CrossRef]
39. Li, L.; Wang, N.; Jin, X.; Deng, R.; Nie, S.; Sun, L.; Wu, Q.; Wei, Y.; Gong, C. Biodegradable and injectable in situ cross–linking chitosan–hyaluronic acid based hydrogels for postoperative adhesion prevention. *Biomaterials* **2014**, *35*, 3903–3917. [CrossRef]
40. Zhao, Y.; Li, Y.; Peng, X.; Yu, X.; Cheng, C.; Yu, X. Feasibility study of oxidized hyaluronic acid cross–linking acellular bovine pericardium with potential application for abdominal wall repair. *Int. J. Biol. Macromol.* **2021**, *184*, 831–842. [CrossRef]
41. Nonsuwan, P.; Matsugami, A.; Hayashi, F.; Hyon, S.H.; Matsumura, K. Controlling the degradation of an oxidized dextran–based hydrogel independent of the mechanical properties. *Carbohydr. Polym.* **2019**, *204*, 131–141. [CrossRef]
42. Zhang, C.; Luo, X.; Wei, T.; Hu, Y.; Li, G.; Zhang, Z. Acylhydrazone bond dynamic covalent polymer gel monolithic column online coupling to high–performance liquid chromatography for analysis of sulfonamides and fluorescent whitening agents in food. *J. Chromatogr. A* **2017**, *1519*, 28–37. [CrossRef] [PubMed]
43. Pandit, A.H.; Mazumdar, N.; Ahmad, S. Periodate oxidized hyaluronic acid–based hydrogel scaffolds for tissue engineering applications. *Int. J. Biol. Macromol.* **2019**, *137*, 853–869. [CrossRef] [PubMed]
44. Ranjan Sarker, S.; Polash, S.A.; Boath, J.; Kandjani, A.E.; Poddar, A.; Dekiwadia, C.; Shukla, R.; Sabri, Y.; Bhargava, S.K. Functionalization of Elongated Tetrahexahedral Au Nanoparticles and Their Antimicrobial Activity Assay. *ACS Appl. Mater. Interfaces* **2019**, *11*, 13450–13459. [CrossRef] [PubMed]
45. Lu, L.; Zhang, J.; Guan, K.; Zhou, J.; Yuan, F.; Guan, Y. Artificial neural network for cytocompatibility and antibacterial enhancement induced by femtosecond laser micro/nano structures. *J. Nanobiotechnol.* **2022**, *20*, 365. [CrossRef]

46. Gangwar, A.; Kumar, P.; Singh, R.; Kush, P. Recent Advances in Mupirocin Delivery Strategies for the Treatment of Bacterial Skin and Soft Tissue Infection. *Future Pharmacol.* **2021**, *1*, 80–103. [CrossRef]
47. Zhang, Y.; Wang, D.; Liu, F.; Sheng, S.; Zhang, H.; Li, W.; Li, Y.; Tian, H. Enhancing the drug sensitivity of antibiotics on drug–resistant bacteria via the photothermal effect of FeTGNPs. *J. Control. Release* **2022**, *341*, 51–59. [CrossRef]